Resonance Raman spectroscopy (n,m)-dependent effects in small-diameter single-wall carbon nanotubes

A. Jorio, C. Fantini, and M. A. Pimenta

Departamento de Física, Universidade Federal de Minas Gerais, Belo Horizonte, MG 30123-970, Brazil

R. B. Capaz

Instituto de Física, Universidade Federal do Rio de Janeiro, Rio de Janeiro, RJ 21941-972, Brazil

Ge. G. Samsonidze, G. Dresselhaus, and M. S. Dresselhaus

Massachusetts Institute of Technology, Cambridge, Massachusetts 02139-4307, USA

J. Jiang, N. Kobayashi, A. Grüneis, and R. Saito

Department of Physics, Tohoku University and CREST JST, Aoba Sendai 980-8578, Japan

This paper presents an accurate analysis of (i) the electronic transition energies E_{22}^S and E_{11}^M, (ii) the radial breathing mode (RBM) frequencies ω_{RBM}, and (iii) the corresponding RBM intensities from 40 small-diameter single-wall carbon nanotubes (SWNTs) in the diameter range $0.7 < d_t < 1.3$ nm. The electronic transition energies (E_{ii}) are initially considered from nonorthogonal tight-binding total-energy calculations. To account for d_t-dependent many-body effects, a logarithmic correction, as proposed by Kane and Mele, is applied to both E_{22}^S and E_{11}^M. The remaining discrepancies between the experimental and theoretical E_{ii} values are shown to be proportional to the chirality-dependent effective masses of electrons and holes, as obtained from the electron energy dispersion relations. Chirality dependent screening effects are also identified in metallic SWNTs. For the RBM frequencies, a small deviation from the linear $1/d_t$ behavior is observed, and this deviation is analyzed based on a chirality-dependent mode softening effect due to nanotube curvature. For those interested in sample characterization, the (n,m) dependence of the resonance intensities is also addressed, the experimental results being compared with theoretical predictions based on matrix elements calculations. This analysis suggests that the (7,5), (7,6), and (6,5) SWNTs are more abundant in sodium dodecyl sulfate wrapped HiPco SWNTs in aqueous solution, in agreement with results previously reported for SWNTs grown by the CoMoCAT or alcohol methods.

I. INTRODUCTION

Optical experiments, such as optical absorption,[1–4] resonance Raman spectroscopy (RRS),[5–15] and photoluminescence (PL),[16–18] have been widely used for single-wall carbon nanotube (SWNT) study and characterization. The plot of the optical transition energies (E_{ii}) as a function of nanotube diameter d_t was introduced in 1999 by Kataura *et al.*,[1] and is commonly called the "Kataura plot." Since then, the Kataura plot has been widely used for the interpretation of optical experiments. In the traditional Kataura plot,[1] the E_{ii} values for the different (n,m) SWNTs were calculated by zone folding the graphene electronic structure, as obtained from a nearest-neighbor tight-binding (TB) model, while the nanotube diameters were obtained by $d_t = a\sqrt{n^2+m^2+nm}/\pi$, where $a = \sqrt{3} \times 0.142$ nm is the graphene lattice constant.[19,20] Although a simple nearest-neighbor TB model is not expected to fully describe the SWNT photophysics,[21] it has been successful for the interpretation of RRS experiments for SWNTs with diameters $d_t > 1.2$ nm.[22] This simple Kataura plot, however, has been shown not to be appropriate for small diameter SWNTs, i.e., for $d_t < 1.2$ nm, where the SWNT curvature causes deviations from the graphene-folded picture, and many-body effects are also shown to become important.[2,3,16,23,24]

Several authors have been searching for a more reliable tight-binding model to describe the optical properties of SWNTs.[4,21,25–27] The tight-binding method can be extended beyond the simplest π-only, orthogonal, nearest-neighbor approximations to include σ electrons, more distant neighbor interactions, and nonorthogonality between basis orbitals.[26,27] Moreover, the tight-binding method can be coupled to interatomic repulsive interactions to allow for the calculation of total energies and structural properties (the so-called tight-binding total-energy method). In this paper, this approach will be called the "extended tight-binding" (ETB) method, to differentiate it from the simplest tight-binding method (sTB) that has been previously applied to the study of large diameter ($d_t > 1.2$ nm) nanotubes. Popov[26] and Samsonidze *et al.*[27] used the ETB parametrization for carbon systems developed by Porezag *et al.*[28] to study many (n,m) SWNTs. After optimization of both bond lengths and bond angles, the E_{ii}^{ETB} and d_t^{ETB} values that account for curvature effects could be calculated for small-diameter SWNTs.[27] The model was shown to nicely reproduce the first (E_{11}^S) and second (E_{22}^S) sets of electronic transition energies for semiconducting SWNTs, as obtained by PL measurements,[16] after including a $1/d_t$ dependent correction ascribed to many-body effects (see Sec. II).[27]

In the present paper (Sec. III), the experimental results (E_{ii}^{RRS}) obtained with resonance Raman spectroscopy (RRS) for SWNTs with diameters in the range $0.7 < d_t < 1.3$ nm are analyzed[29] by using the ETB (E_{ii}^{ETB}) model.[27] The discrepancies between the experimental E_{ii}^{RRS} and the calculated E_{ii}^{ETB} values $\Delta E_{ii} = (E_{ii}^{\mathrm{RRS}} - E_{ii}^{\mathrm{ETB}})$ are then analyzed within the framework of many-body effects and their dependence on SWNT geometry. Diameter *and* chirality dependences are observed, as well as a dependence on semiconducting SWNT type I [$\mathrm{mod}(2n+m,3)=1$] vs type II [$\mathrm{mod}(2n+m,3)=2$].

In Sec. IV the relation between the observed radial breathing mode frequencies ω_{RBM} and the d_t for each (n,m) SWNT is also analyzed. The ω_{RBM} is found to deviate from the simple $1/d_t$ behavior, and this deviation is analyzed considering the RBM softening due to the nanotube curvature. In the end, we obtain an accurate [E_{ii} vs ω_{RBM}] plot, and the corresponding Kataura plot [E_{ii} vs d_t] for the interpretation of optical-absorption, PL, and RRS experiments on SWNTs, applicable to small-diameter SWNTs ($0.7 < d_t < 1.2$ nm). The model is also extended to larger diameter SWNTs ($d_t > 1.2$ nm), and it is shown to be consistent with previously published RRS data[5–15] (Sec. V).

Finally, for the researchers more interested in sample characterization, Sec. VI compares the experimentally obtained RBM RRS intensities with theoretical predictions based on matrix elements calculations, that also show an (n,m) dependence. These results are intended to shed light on the use of resonance Raman spectroscopy to characterize (n,m) populations within a SWNT sample.

II. BACKGROUND FOR THE EXPERIMENTAL AND THEORETICAL ANALYSIS

The sample measured by RRS consists of SDS (sodium dodecyl sulfate) wrapped HiPco SWNTs dispersed in aqueous solution, as described in Ref. 16. A Dilor *XY* triple-monochromator spectrometer and a tunable laser system which allows an almost continuous change of the excitation laser energies (E_{laser}) in the range between 1.52 and 2.71 eV was used.[29] This quasicontinuous variation of E_{laser} provides detailed information about the resonance window (Raman intensity as a function of E_{laser}), thus giving ($E_{ii}, \omega_{\mathrm{RBM}}$) experimental values for 40 different (n,m) SWNTs, including 22 semiconducting SWNTs in resonance with E_{22}^S and 18 metallic SWNTs in resonance with E_{11}^M. The frequency determination of ω_{RBM} is directly given in the Raman spectra with an accuracy of ± 1.0 cm^{-1}. The electronic transition energy determination of E_{ii} is obtained by analyzing the Stokes and anti-Stokes resonance windows for each RBM peak, as discussed in Ref. 29, and the accuracy is better than ± 10 meV. These experimental accuracies are confirmed by comparing the ($\omega_{\mathrm{RBM}}, E_{ii}$) result published by Telg *et al.*[30] for different semiconducting (n,m) SWNTs. For metallic SWNTs, Refs. 29 and 30 show discrepancies larger than the experimental accuracy, and these results will be discussed in Sec. IV.

The (n,m) assignment is based on the experimentally obtained ($E_{ii}, \omega_{\mathrm{RBM}}$) plots which show $(2n+m)=$ constant family patterns,[29] and the RRS-derived results, thus obtained, are
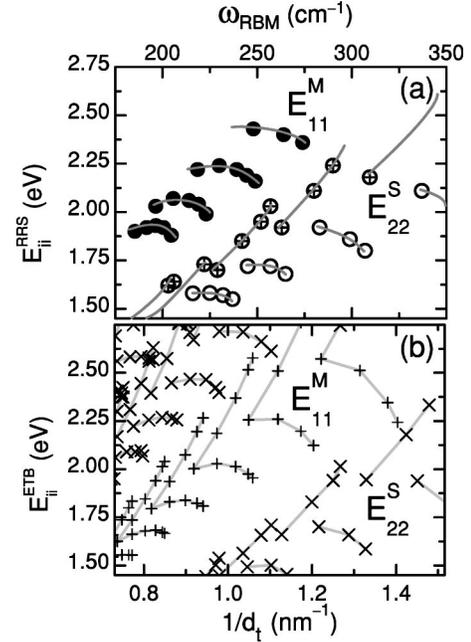
FIG. 1. (a) The electronic transition energies for SWNTs as observed by RRS (E_{ii}^{RRS}) vs radial breathing mode frequency (ω_{RBM}). ● stand for metallic, ○ for type-I, and ⊕ for type-II semiconducting SWNTs. (b) The electronic transition energies calculated by the ETB (E_{ii}^{ETB}) from Ref. 27 (crosses for semiconducting and pluses for metallic SNWTs) vs $1/d_t$. The gray lines connect SWNTs belonging to the same $(2n+m)=$ const family.

in agreement with previously proposed (n,m) assignments for semiconducting SWNTs wrapped in SDS, based on PL measurements.[16]

Figure 1 presents actual RRS experimental (a) and theoretical (b) results for the E_{ii} values. The symbols that are used for the experimental results in Fig. 1(a), i.e., (●) for metallic, (○) for type-I, and (⊕) for type-II semiconducting SWNTs (see caption), are also used elsewhere in the paper. The theoretical E_{ii}^{ETB} values come from tight-binding total-energy calculations (ETB model).[27] The comparison between the RRS experimental E_{ii}^{RRS} and ETB-based theoretical E_{ii}^{ETB} results in Fig. 1 shows that the theoretical results are red-shifted from the experimental RRS data, as previously observed.[27] This redshift, ascribed to many-body effects,[2,3,16,23,24,27,31] is the subject of the next section. For metallic SWNTs, although two E_{11}^M values are expected for each SWNT due to the trigonal warping effect,[32] only the lower E_{11}^M component is observed experimentally[29] for measurements of the RBM feature.

III. ANALYSIS OF MANY-BODY EFFECTS ON THE ELECTRONIC TRANSITION ENERGIES E_{ii}

A. Diameter dependence

First-principles calculations[24,33] suggest that the one-dimensional (1D) nature of semiconducting SWNTs leads to much stronger many-body effects as compared to bulk semiconductors. Many-body effects in semiconducting SWNTs can be described by a positive shift of the band gap due to
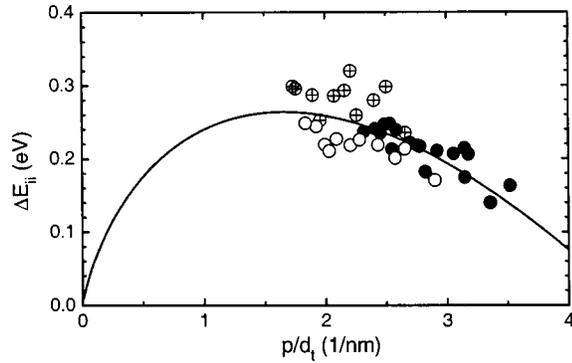
FIG. 2. Energy differences (ΔE_{ii}) between the experimentally obtained E_{ii}^{RRS} values and the corresponding ETB calculated values as a function of p/d_t. $\Delta E_{22}^S = E_{22}^{S(\text{RRS})} - E_{22}^{S(\text{ETB})}$ is given by open circles (type I) and by circles with "+" signs ($\oplus$) (type II), and $\Delta E_{11}^M = E_{11}^{M(\text{RRS})} - E_{11}^{M(\text{ETB})}$ is given by filled circles ($\bullet$). The solid line represents the diameter-dependent logarithmic correction $E^{\ln}(d_t)$ that is fit to the armchair data ($\theta = 30°$) and separates the type-I and type-II semiconducting SWNTs, as given by Eq. (1).

electron-electron (quasiparticle) interactions and a negative shift of the optical band gap due to electron-hole (exciton) interactions. These two large shifts tend to cancel each other to some extent. Kane and Mele (KM) (Ref. 31) proposed that, as a result of this partial cancellation, the many-body corrections in the band gap of nearly armchair ($\theta \sim 30°$) semiconducting SWNTs could be described by a theory of a two-dimensional graphene sheet, where the Coulomb interaction leads to a relatively smaller correction to the E_{ii} values, with a nonlinear (logarithmic) diameter dependence.

When analyzing experimental data, KM (Ref. 31) for simplicity considered the single-particle models to exhibit a linear p/d_t dependence for the nearly armchair SWNTs. Here $p = 1, 2, 3, 4, \ldots$ is for $E_{11}^S, E_{22}^S, E_{11}^M, E_{33}^S, \ldots$, respectively. However, the E_{ii} dependence on (p/d_t) is linear only in the limit of large diameter tubes (d_t above 1.2 nm). Figure 2 plots the deviation (ΔE_{ii}) of the RRS data (E_{ii}^{RRS}) from the calculated E_{ii}^{ETB} as a function of p/d_t. The solid line in Fig. 2 represents the explicit diameter-dependent logarithmic correction $E^{\ln}(d_t)$ of KM (Ref. 31) that comes from fitting ΔE_{ii} to the data points for the near armchair SWNTs ($\theta \simeq 30°$), as given by

$$E^{\ln}(d_t) = 0.55 \left(\frac{2p}{3d_t} \right) \ln \left[3 \left/ \left(\frac{2p}{3d_t} \right) \right. \right] \tag{1}$$

thus separating the type-I and type-II semiconducting SWNTs. By considering the case $\theta \simeq 30°$, the dependence on chiral angle is suppressed. The KM correction therefore accounts for the *diameter* dependent many-body effects.

KM (Ref. 31) showed that ΔE_{11}^S and ΔE_{22}^S, as measured by PL, both follow the same logarithmic dependence on p/d_t. Figure 2 shows that metallic SWNTs behave similarly to both semiconducting type-I and type-II SWNTs. The same $E^{\ln}(d_t)$ correction also fits the E_{11}^M for armchair SWNTs both in functional form and the numerical fitting parameters. The ability of KM's correction term $E^{\ln}(d_t)$ to fit the optical transitions for both semiconducting and metallic SWNTs is intriguing. The many-body effects are expected to be much stronger in semiconducting SWNTs (order of 1 eV),[24] since in the case of metallic SWNTs, the screening by free electrons is expected to reduce the many-body effects (to ~ 0.1–0.3 eV). This result must be related to the near cancellation of the large quasiparticle and excitonic corrections in semiconducting SWNTs, resulting on a small effect (order of 0.1 eV) similar to the case of metallic tubes.

B. Chirality dependence

1. Semiconducting SWNTs

The solid line in Fig. 2 represents the diameter-dependent logarithmic correction in Eq. (1). The spread from this solid line (± 70 meV) shows the chirality dependence of E_{ii} that is not fully handled within the one-electron ETB picture. Figure 3(a) plots the discrepancies between the experimental results $E_{22}^{S(\text{RRS})}$ and theoretical calculations that remain after correcting the one-electron energies $E_{22}^{S(\text{ETB})}$ for the diameter-dependent logarithmic many-body correction $E^{\ln}(d_t)$ of Eq. (1). The remaining deviation of $[E_{22}^{S(\text{RRS})} - E_{22}^{S(\text{ETB})} - E^{\ln}(d_t)]$ from the zero line should reflect a chiral angle dependence of the many-body corrections.

Figure 3(b) shows the electron effective masses $m_2^S(n,m)$ for the semiconducting SWNTs that are calculated by differentiating the $E(k)$ energy dispersion relations obtained by ETB, at the van Hove singularity (vHS) k_2 point for E_{22}^S. The effective masses depend on both diameter *and* chiral angle. A functional form for $m_i^S(d_t, \theta)$ that accounts for both the diameter and chirality-dependent curvature effects on the effective masses can be obtained by fitting the calculated $m_i^S(n,m)$ with

$$m_i^S(d_t, \theta) = A_i^S/d_t + B_i^S/d_t^2 + C_i^S \cos 3\theta/d_t + D_i^S \cos 3\theta/d_t^2. \tag{2}$$

The parameters that fit the calculated $m_i^S(n,m)$ data are shown in Table I for E_{11}^S and E_{22}^S semiconducting SWNTs.

The chirality dependence of $m_2^S(n,m)$ gives the deviation from the armchair line $m_2^S(d_t, \theta = 30°)$ fitted by

$$m_2^S(d_t, \theta = 30°) = A_2^S/d_t + B_2^S/d_t^2, \tag{3}$$

and shown in Fig. 3(b) by the solid line. The deviation is larger for smaller chiral angles ($\theta \simeq 0$, near zigzag), and it is opposite in sign for type-I ($\bigcirc$) as compared to type-II ($\oplus$) semiconducting SWNTs, showing also a $(2n+m) = $ const family dependence.

The family patterns in Fig. 3(a) are similar to those in Fig. 3(b), showing a correlation between the data points for $[E_{22}^{S(\text{RRS})} - E_{22}^{S(\text{ETB})} - E^{\ln}(d_t)]$ and for the effective mass as a function of $1/d_t$ for the individual SWNTs, as shown in Fig. 3(c). The similarity between the experimental results [Fig. 3(a)] and the chirality-dependent effective masses [Fig. 3(b)] is clearer after subtracting the linear $m_2^S(d_t, \theta = 30°)$ function [Eq. (3)] that corrects the diameter dependence of the effective masses for (near) armchair SWNTs ($\theta \sim 30°$). From the slope of the line fitting the data points in Fig. 3(c) we obtain
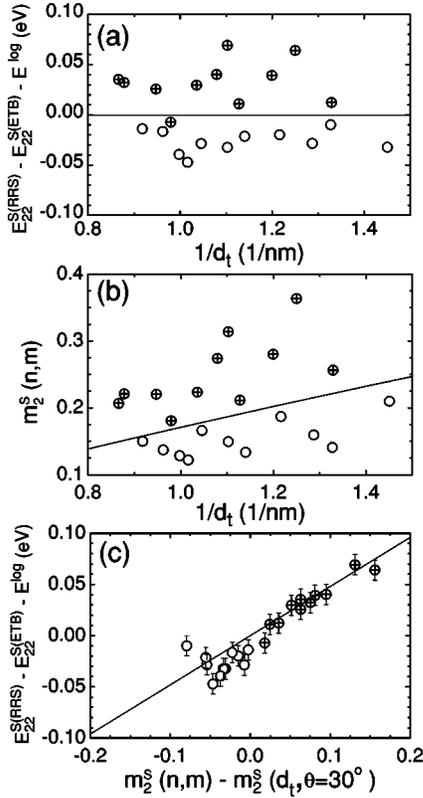
FIG. 3. (a) The remaining deviation of the experimental results for $E_{22}^{S(RRS)}$ from the theoretical values calculated by ETB ($E_{22}^{S(ETB)}$), after correcting for the diameter-dependent many-body effects [$E^{ln}(d_t)$], which follows from Fig. 2, as a function of $1/d_t$. ($\bigcirc$) and ($\oplus$), respectively, stand for type-I and type-II semiconducting SWNTs. The solid line just shows the zero line, making clear the different behaviors for type-I and type-II semiconducting SWNTs. (b) Effective masses $m_2^S(n,m)$ for the E_{22}^S electrons for the different (n,m) SWNTs as a function of $1/d_t$. The solid line gives the extrapolated $m_2^S(d_t, \theta=30°)$ for "hypothetical" armchair ($\theta=30°$) semiconducting SWNTs, separating type-I and type-II $m_2^S(n,m)$ values. Here "hypothetical" is used to denote semiconducting SWNTs with $\theta \sim 30°$ since actual armchair SWNTs are all metallic. The solid line in (b) comes from Eq. (3), with A_2^S and B_2^S values averaged between type-I and type-II semiconducting SWNTs in Table I. (c) The remaining chirality-dependent deviation [$E_{22}^{S(RRS)} - E_{22}^{S(ETB)} - E^{ln}(d_t)$] as a function of the respective effective-mass deviation from $m_2^S(d_t, \theta=30°)$. The data from 22 different (n,m) SWNTs have been considered. The solid line is a linear fit to the data points (see text).

the proportionality constant between the experimental results in Fig. 3(a) and the effective masses in Fig. 3(b) at constant diameter, thus giving an effective-mass-dependent correction E_{22}^{EMC},

$$
\begin{aligned}
E_{22}^{EMC} &= E_{22}^{S(RRS)} - E_{22}^{S(ETB)} - E^{ln}(d_t) \\
&= (0.48 \pm 0.04)[m_2^S(n,m) - m_2^S(d_t, \theta=30°)] \\
&= (0.48 \pm 0.04)(C_2^S \cos 3\theta/d_t + D_2^S \cos 3\theta/d_t^2) \quad (4)
\end{aligned}
$$

which is shown by the solid line in Fig. 3(c). The proportionality between the chirality dependence of the many-body cor-

rections and effective masses provides a useful and simple way to estimate the former. Interestingly, Perebeinos *et al.*[34] have proposed a power-law dependence of the exciton binding energies on the effective masses. If the total many-body corrections display a similar scaling behavior, the proportionality expressed in Eq. (4) will follow naturally (provided that chirality-dependent corrections to the masses are small).

Although many-body effects also depend on the effective mass of the valence band (holes), only the effective masses for the conduction band (electrons) were explicitly considered for simplicity in constructing Fig. 3 and fitting Eq. (4). The effective masses for the valence band in the diameter region considered here are about 10% larger, and the chirality dependence is similar. This difference between the effective masses in the valence and conduction bands gives evidence for a small asymmetry between the subband energies with respect to the Fermi level, that has not yet been characterized experimentally.

The reason why the effective masses depend on whether the semiconducting SWNT is type I or type II is due to the trigonal warping effect of the electronic structure.[32] Figures 4(a) and 4(b) show the trigonally distorted equienergy contours in the region of the 2D graphene Brillouin zone close to the K point, where the optical processes occur. The parallel lines are the cutting lines for the allowed wave vectors for a type-I [Fig. 4(a)] and a type-II [Fig. 4(b)] zigzag SWNTs. E_{11}^S belongs to the cutting line closest to the K point, and E_{22}^S belongs to the second-closest cutting line, the vHSs appearing where the cutting line is tangent to an equienergy contour. Therefore the difference between type-I and type-II SWNTs is given by the position of the vHSs with respect to the 2D Brillouin zone, E_{22}^S appearing in the $K-M$ direction for type-I SWNTs, and in the $K-\Gamma$ direction for type-II SWNTs. Figure 4(c) presents the first and second conduction bands for the type-I (solid line) and type-II (dashed line) SWNTs shown in Figs. 4(a) and 4(b), respectively. Because of the trigonal distortion of the equienergy contours in the 2D Brillouin zone, the effective masses will be different for type-I and type-II SWNTs.

Finally, the chirality dependence of the effective masses can also be understood, since the chirality determines the angle of the cutting lines with respect to the trigonally distorted equienergy contours. Figure 4 is made for zigzag SWNTs, where the difference between type-I and type-II semiconducting SWNTs is a maximum. In the case of hypothetical armchair semiconducting SWNTs, the cutting lines are both parallel to an edge $(K-M)$ of the hexagonal 2D Brillouin zone, and there is no difference between the type-I and type-II electronic dispersions in this case.

2. Metallic SWNTs

The same analysis, developed above for semiconducting E_{22}^S transitions, can be applied to the E_{11}^M transitions for metallic SWNTs. In this context, Fig. 5(a) plots the $1/d_t$ dependence for [$E_{11}^{M(RRS)} - E_{11}^{M(ETB)} - E^{ln}(d_t)$], while Fig. 5(b) plots the $1/d_t$ dependence for the calculated effective masses $m_1^M(n,m)$ of the lower energy E_{11}^M electrons. Figure 5(c) plots the experimental points in Fig. 5(a) as a function of the effective masses in Fig. 5(b) after subtracting for $m_1^M(d_t, \theta$

TABLE I. Fitting parameters of [Eq. (2)] for the effective masses $m_i^S(n,m)$ of electrons and holes in semiconducting SWNTs. Here $i=1,2$ are related to E_{11}^S and E_{22}^S, respectively. Type stands for type-I and type-II semiconducting SWNTs based on $(2n+m)$ families. Fitting parameters for the effective masses $m_i^M(n,m)$ of metallic SWNTs are also given (see Sec. III B).

i	type	A_i^S (nm)	B_i^S (nm^2)	C_i^S (nm)	D_i^S (nm^2)
Electron					
1	I	0.0825	0.0159	−0.0067	0.0253
2	I	0.181	−0.00885	−0.0109	−0.0422
1	II	0.0813	0.0172	0.0121	−0.0388
2	II	0.186	−0.0169	−0.0612	0.172
Hole					
1	I	0.0799	0.0235	−0.00791	0.0243
2	I	0.181	0.00680	−0.00402	−0.0566
1	II	0.0794	0.0239	0.0155	−0.0445
2	II	0.179	0.00662	−0.0678	0.185
i		A_i^M (nm)	B_i^M (nm^2)	C_i^M (nm)	D_i^M (nm^2)
Electron					
1		0.278	−0.0403	−0.0436	−0.0407
Hole					
1		0.279	−0.0116	−0.0299	−0.0712

$=30°$) [solid line in Fig. 5(b)]. Surprisingly, the dependence is opposite for metallic SWNTs relative to semiconducting SWNTs [see Fig. 3(c)], with the remaining deviation $[E_{11}^{M(RRS)} - E_{11}^{M(ETB)} - E^{ln}(d_t)]$ *decreasing* with increasing effective-mass deviation $m_1(n,m) - m_1(d_t, \theta=30°)$. The data in Fig. 5(c) are fit to give

$$
\begin{aligned}
E_{11}^{EMC} &= E_{11}^{M(RRS)} - E_{11}^{M(ETB)} - E^{ln}(d_t) \\
&= (-0.19 \pm 0.05)[m_1^M(n,m) - m_1^M(d_t, \theta = 30°)] \\
&= (-0.19 \pm 0.05)(C_1^M \cos 3\theta/d_t + D_1^M \cos 3\theta/d_t^2),
\end{aligned}
$$
(5)

where $m_1^M(n,m)$ and $m_1^M(d_t, \theta=30°)$ are given by the same functional forms as in Eqs. (2) and (3) for semiconducting SWNTs, with the parameters for electrons in metallic SWNTs given in Table I.

In the case of metallic SWNTs, RBM peaks have only been observed in the Raman spectra for the lower E_{11}^M branch, which is formally equivalent to observing only type-I semiconducting SWNTs. A possible reason why the higher E_{11}^M peaks are absent in the experiment is the suppression of the two one-particle levels and the enhancement of one excitonic level due to the so called "f-sum rule," which requires the total oscillator strength to be conserved.[24,35]

In the context of many-body effects, the negative slope observed in Fig. 5(c) can be related to a chirality dependent screening by free electrons. It is known that only armchair SWNTs are truly metallic, while a minigap (of a few meV) appears in chiral and zigzag tubes because of the SWNT curvature effect.[19,20] This minigap increases with decreasing chiral angle, being a maximum for zigzag SWNTs. Therefore one can expect that the screening effect will be a maximum for armchair SWNTs, decreasing with decreasing chiral angle, and being a minimum for zigzag tubes. In the case of armchair SWNTs, the many-body related blueshift is given by $E^{ln}(d_t)$, as obtained in Sec. III A. For smaller chiral angle SWNTs, however, the correction is higher than $E^{ln}(d_t)$ due to the smaller screening, thus giving the negative slope in Fig. 5(c).
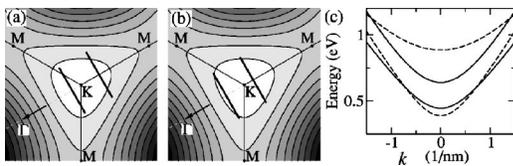
FIG. 4. (a), (b) 2D graphene Brillouin zone close to the K point, showing the trigonally distorted equienergy contours. The parallel lines are the cutting lines for the allowed wave vectors for type-I (a) and type-II (b) zigzag semiconducting SWNTs. (c) First and second conduction bands for type-I (solid line) and type-II (dashed line) semiconducting zigzag SWNTs shown in (a) and (b), respectively.

IV. ANALYSIS OF THE RADIAL BREATHING MODE FREQUENCIES ω_{RBM}

For the analysis of RRS data with the Kataura plot, it is important to establish the relation between the SWNT diameter and the RBM frequencies (ω_{RBM}). Figure 6(a) shows a plot of the deviation of ω_{RBM} from the best linear $1/d_t$ dependence that fits all the experimental data $[\Delta\omega_{RBM}=\omega_{RBM} - (218.3/d_t+15.9)]$ as a function of d_t. Figure 6(b) shows the same quantity as a function of the chiral angle θ. In both plots, one clearly sees deviations of the points from the
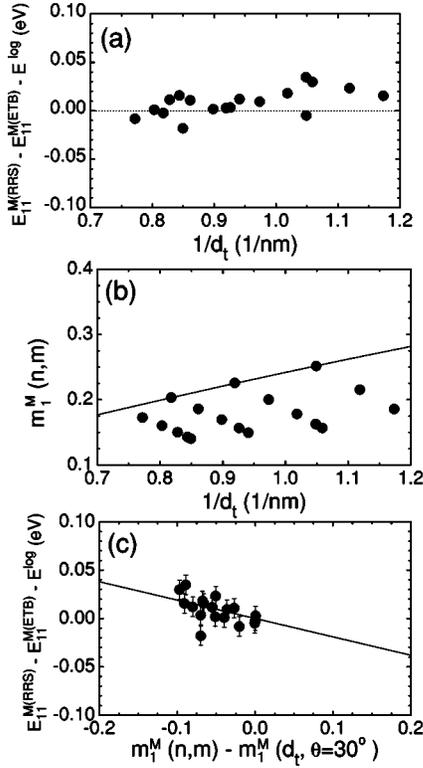
FIG. 5. (a) The remaining deviation of the experimental results for $E_{11}^{M(RRS)}$ for metallic SWNTs from the theoretical values calculated by ETB ($E_{11}^{M(ETB)}$), after correcting for the diameter dependent many-body effects [using the same $E^{ln}(d_t)$ function as in Eq. (1) for semiconducting SWNTs], plotted here as a function of $1/d_t$. The dotted line is given to show the deviation from the $[E_{11}^{M(RRS)} - E_{11}^{M(ETB)} - E^{ln}(d_t) = 0]$ line. (b) Effective masses $m_1^M(n,m)$ for the lower energy E_{11}^M electrons of different (n,m) SWNTs as a function of $1/d_t$. The solid line gives the extrapolated $m_1^M(d_t, \theta=30°)$ for armchair metallic SWNTs. (c) The solid points give the remaining deviation $[E_{11}^{M(RRS)} - E_{11}^{M(ETB)} - E^{ln}(d_t)]$ as a function of the respective effective-mass deviation from $m_1^M(d_t, \theta=30°)$ for the 18 metallic tubes that were measured. The solid line is a fit to the data [see Eq. (5)].

$\Delta\omega_{RBM} = 0$ line as large as ~ 3 cm^{-1}, and these deviations are larger than the experimental accuracy ($\simeq 1.0$ cm^{-1}).

Several interesting trends can be seen from the deviations in Figs. 6(a) and 6(b). The first one is the observation of systematically larger $\Delta\omega_{RBM}$ for metallic SWNTs when compared with semiconducting ones of similar diameter. The second is a $\Delta\omega_{RBM}$ dependence on the chiral angle, showing a clear decrease in $\Delta\omega_{RBM}$ with decreasing θ from 30° (armchair) to 0° (zigzag) for both metallic and semiconducting tubes. No type-I vs type-II dependence in ω_{RBM} is observed for semiconducting SWNTs.

Some of these deviations in ω_{RBM} are due to curvature effects. For small-diameter SWNTs, curvature weakens the chemical bonds which have components along the circumference, because of sp^2-sp^3 mixing. As a result, the SWNT diameter increases and the RBM frequency decreases with respect to their ideal values. Moreover, curvature destroys the isotropy of the elastic constants in SWNTs and therefore introduces a chirality dependence into ω_{RBM}. All these ef-
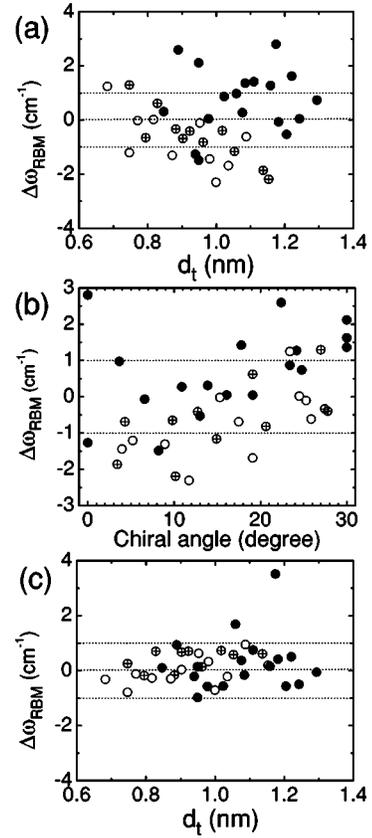
FIG. 6. (a) Deviation of the experimentally observed RBM frequency (ω_{RBM}) from the linear dependence given by $(218.3/d_t + 15.9)$, as a function of d_t. (b) Deviation of ω_{RBM} from $(218.3/d_t + 15.9)$, as a function of θ. (c) Deviation of ω_{RBM} from the $\omega_{RBM}^{calc}(d_t, \theta)$ given by Eq. (6), as a function of d_t. In (a), (b), and (c), open, crossed, and filled circles denote semiconducting type-I, type-II, and metallic SWNT's, respectively. The dotted lines show the experimental accuracy of ± 1 cm^{-1}. In (c), only two small chiral angle metallic (15, 0) and (13, 1) SWNTs lie outside the experimental accuracy range.

fects are well documented from a theoretical point of view[27,38] where, by allowing the atoms to assume equilibrium positions for each (d_t, θ), the effective diameter changes.

To describe the differences between metallic vs semiconducting SWNTs regarding the curvature *and* chirality dependences of the experimental RBM data, we propose the following functional form:

$$\omega_{RBM}^{calc} = A/d_t + B + (C + D\cos^2 3\theta)/d_t^2. \quad (6)$$

Semiconducting and metallic data are fit separately, and the fitting parameters obtained are shown in Table II. The results for $\Delta\omega_{RBM} = \omega_{RBM}^{EXP} - \omega_{RBM}^{calc}(d_t, \theta)$ are shown as a function of diameter in Fig. 6(c). All the $\Delta\omega_{RBM}$ points, except those for two low chiral angle metallic SWNTs, fall close to zero, inside the experimental accuracy of ± 1 cm^{-1}. Furthermore, for larger diameter SWNTs, i.e., with diameters in the range 1.2–2.0 nm, ω_{RBM} obtained by Eq. (6) and by the relations $\omega_{RBM} = 248/d_t$ (Ref. 39) or $\omega_{RBM} = 234/d_t + 10$ (Ref. 9) do not

TABLE II. Fitting parameters for the radial breathing mode frequency ω_{RBM} as a function of diameter and chiral angle, as given by Eq. (6), for 22 semiconducting and 18 metallic SWNTs wrapped in SDS in an aqueous solution.

	A (cm^{-1} nm)	B (cm^{-1})	C (cm^{-1} nm^2)	D (cm^{-1} nm^2)
Semicon.	227	7.3 ± 0.3	-1.1 ± 0.3	-0.9 ± 0.2
Metallic	227	11.8 ± 1.0	-2.7 ± 1.2	-2.7 ± 0.8

differ by more than the parameter B, that is ascribed to environmental effects, as discussed below. Therefore the functional form for ω_{RBM}^{calc} given in Eq. (6) with the parameters from Table II not only describes the ω_{RBM} observed for HiPco SWNTs wrapped by SDS within the experimental precision, but ω_{RBM}^{calc} also converges to functional forms in the literature,[5-7,9,10] for larger diameter tubes $d_t > 1.2$ nm.

Physical interpretations can be given to all parameters of Eq. (6). Based on the results obtained from the fit, the following comments can be made:

(i) A describes the elastic behavior of an isolated SWNT in the large-diameter limit, where the elasticity theory, which gives $A = 227$ cm^{-1} nm,[36,37] is expected to be valid.

(ii) B accounts for the interaction between the SWNT and its SDS wrapping. The value of B is larger for metallic SWNTs compared to semiconducting SWNTs, thus yielding a systematically higher $\Delta\omega_{RBM}$ for metallic SWNTs when compared with semiconducting SWNTs and indicating a stronger interaction between SDS and metallic SWNTs. This result is consistent with the observation of no change in ω_{RBM} for semiconducting SWNTs between SDS wrapped and bundled SWNTs,[29] while a small change (~ 2 cm^{-1} lower in bundles) is observed for metallic tubes. A smaller difference for ω_{RBM} between metallic and semiconducting SWNTs was observed by Telg et al.,[30] in better agreement with our measurement on HiPco bundles.[29] This result may be related to differences in the samples.

(iii) C and D account for (chirality-dependent) curvature effects. $C < 0$ results in the overall softening of ω_{RBM} due to the increase in curvature, as expected. $D < 0$ accounts for an even more pronounced softening for zigzag tubes with respect to armchair SWNTs, in agreement with theory.[27,38] Interestingly, the RBM curvature-related softening is clearly larger for metallic tubes (more negative values of C and D), also in agreement with theoretical calculations for isolated SWNTs, where metallic SWNTs generally exhibit lower frequencies.[27,38] For metallic SWNTs within $d_t = 1$ nm, Kürti et al.[38] predict a ~ 5-cm^{-1} spread with chirality, while a ~ 3 cm^{-1} was obtained experimentally. It is interesting to recall that, similar to the ω_{RBM} behavior, the G^- frequencies in metallic SWNTs also show a larger curvature-induced softening as compared to semiconducting SWNTs.[40] The two effects are probably related, since both modes involve bond-stretching along the circumference.

The chirality dependence of ω_{RBM} deserves a deeper understanding. Kürti et al.[38] describe in detail the curvature effects on many structural properties of SWNTs. For instance, it is predicted that diameter deviations from the ideal d_t values are roughly the same for zigzag and armchair tubes,
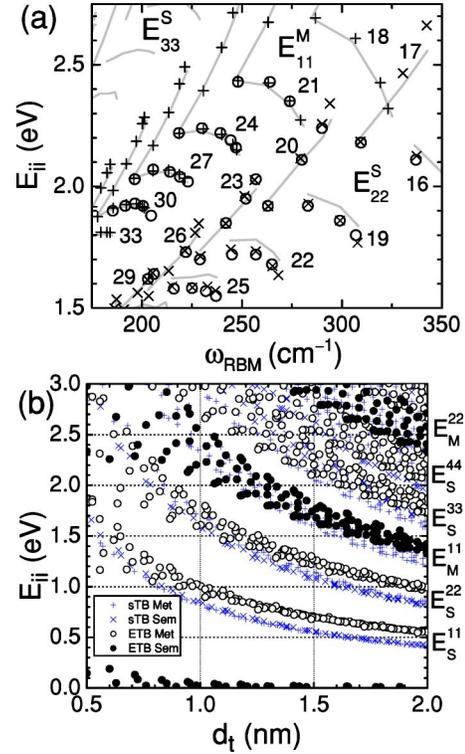
FIG. 7. (a) The revised (E_{ii} vs ω_{RBM}) plot comparing experimental results from RRS experiments on SDS wrapped SWNTs in solution (circles) with the predictions of Eqs. (6) and (7) (pluses and crosses). The numbers give $(2n+m)$ for the SWNT families shown by the gray lines. (b) The revised Kataura plot (black open and filled circles) is compared with the previously used nearest-neighbor Kataura plot (blue pluses and crosses and $\gamma_0 = 2.89$ eV, Ref. 41).

but the changes in bond lengths are larger for the two C-C bonds with components along the circumference for zigzag tubes as compared to the three such bonds for armchair tubes with similar diameter. This is a purely geometric effect, related to the directions of the three C-C bonds with respect to the circumferential direction. Therefore, in armchair tubes, the circumferential strain is more evenly distributed between the bonds, leading to smaller bond elongations. Since the RBM softening is directly related to the elongation of bonds along the circumference, a larger softening of ω_{RBM} for zigzag tubes relative to armchair tubes is expected.

V. KATAURA PLOT

Having obtained an accurate model for the electronic transition energies and radial breathing mode frequencies, a Kataura plot can be made and compared with experimental results and other theoretical models.

The optical transition energies E_{11}^S, E_{22}^S, and E_{11}^M can be obtained considering

$$E_{11}^S = E_{11}^{S(ETB)} + E^{ln}(d_t) + E_{11}^{S(EMC)},$$

$$E_{22}^S = E_{22}^{S(ETB)} + E^{ln}(d_t) + E_{22}^{S(EMC)},$$

$$E_{11}^M = E_{11}^{M(\text{ETB})} + E^{\ln}(d_t) + E_{11}^{M(\text{EMC})}. \qquad (7)$$

E_{11}^{EMC} has not been obtained experimentally but, as a first approximation, Eqs. (4) can be used with the effective mass parameters for E_{11}^S in Table I. For higher E_{ii} transitions (E_{33}^S, E_{44}^S, E_{22}^M, etc.) the $E^{\ln}(d_t)$ diameter dependent correction does not work since the energies are higher than the cutoff energy, that gives the point where the logarithmic correction becomes negative.[31] Since there is no good set of experimental data presently available for an accurate determination of the many-body corrections for these E_{ii}^S and E_{ii}^M energies, we just use as a first approximation, the linear functions $\Delta E_{ii}^S = (0.38 - 0.12 \text{ nm}/d_t)$ eV and $\Delta E_{ii}^M = (0.42 - 0.22 \text{ nm}/d_t)$ eV, that fit ΔE_{22}^S and ΔE_{11}^M, respectively, reasonably well.

Figure 7(a) is what we call a revised plot of E_{ii} vs ω_{RBM}. Here E_{ii}^{RSS} shown by open circles are compared with E_{ii} as calculated from Eq. (7) (pluses and crosses), and the conversion from d_t to ω_{RBM} considers the functional form given in Eq. (6). The gray lines trace the $E_{ii}^{\text{ETB}} + E^{\log}(d_t)$ values, without considering E_{ii}^{EMC}, thus showing the effect of the effective-mass correction on E_{ii} when comparing with the position for the pluses and crosses. The agreement between theory and experiment seen in Fig. 7(a) is within experimental precision.

In Fig. 7(b) the revised Kataura plot (E_{ii} given by black open and filled circles) is compared with the previously used nearest-neighbor simple Kataura plot (E_{ii}^{sTB} given by blue pluses and crosses), parametrized for RRS experiments, with $\gamma_0 = 2.89$ eV.[41,42] Here the optimized diameters d_t are used.[27] The results are extended to the larger diameter region ($1 < d_t < 2$ nm), where the previous Kataura plot has been successfully used to interpret RRS data. In general, the revised E_{ii} is observed to be higher than E_{ii}^{sTB}. However, previous RRS results for E_{11}^M have been obtained for SWNTs with diameters roughly around 1.3-1.5 nm, where there is good agreement between the revised E_{ii} and the simple TB calculations. It is important to note that E_{11}^M measurements have provided much important data for RRS TB parametrization.[39,42] The blueshift of the revised E_{ii} in comparison with E_{ii}^{sTB} is only significant below 1.5 eV, that is, out of the range of usual lasers used for RRS experiments. For semiconducting SWNTs, a blueshift for E_{22}^S values is observed for $d_t > 1.2$ nm, again corresponding to E_{22}^S values lower than 1.5 eV. Experimental data are only available for E_{22}^S values higher than 1.5 eV, i.e., for $d_t < 1.2$ nm,[9,22,39] where the revised E_{ii} and E_{ii}^{sTB} are roughly coincident. Furthermore, there are no optical experimental data available for large diameter SWNTs in resonance with E_{11}^S, but data are only available for low-diameter tubes.[15–17] Therefore the model presented here is consistent with all previously published RRS experimental results.

VI. ANALYSIS OF THE RESONANCE WINDOW INTENSITIES *I*

In the procedure used to characterize the SWNTs produced by a given synthesis process, the Kataura plot in Fig. 7 is important for the identification of the (n,m) species present in the sample. However, for the characterization of the amount of a given (n,m) in the sample measured by PL or RRS, it is not correct just to analyze the respective intensity of the PL or RRS peak. It is also important to analyze the (n,m) dependence of the PL or RRS cross sections.

The first-order Stokes Raman intensity per tube length for the RBM features is calculated from[43]

$$I_{i,f}(E_\ell)/C = \left| \int \frac{M^{\text{opt}}(k) M^{\text{e-ph}}(k) M^{\text{opt}}(k)}{[E_f(k) - E_i(k) - E_\ell + i\gamma][E_f(k) - E_i(k) - E_\ell + \hbar\omega_{\text{RBM}} + i\gamma]} dk \right|^2, \qquad (8)$$

where C is a normalization intensity factor, E_ℓ is a short form of E_{laser}, while $M^{\text{opt}}(k)$ and $M^{\text{e-ph}}(k)$ are the electron-photon and electron-phonon matrix elements. $M^{\text{opt}}(k)$ and $M^{\text{e-ph}}(k)$ are calculated within the tight-binding scheme,[44] considering all the electrons with wave vector k and the RBM with $q = 0$, and the results are consistent with *ab initio* calculations.[45] In the calculation, the laser energy is set to $E_\ell = E_{22}^{S(\text{RRS})}$ and $E_\ell = E_{11}^{M(\text{RRS})}$ for semiconducting and metallic nanotubes, respectively. The lifetime γ is chosen to be 60 meV, which is the average experimental value for the RRS windows measured for SDS wrapped SWNTs in aqueous solution.[29]

The results thus obtained are shown in Fig. 8 for the RBM intensity dependence on d_t (a) and on θ (b), and the results are calculated per unit length. The (n,m) intensities show an interesting dependence related to the different SWNT families. For example, in Fig. 8(a), points of almost constant intensity are related to $(n-m) = \text{const}$ families. Points for $(2n+m) = \text{const}$ families form patterns departing from low intensities up to higher intensities, zigzag SWNTs exhibiting larger intensities than armchair tubes. The opposite family behavior is observed in Fig. 8(b), i.e., $(2n+m) = \text{const}$ SWNTs exhibit very similar intensities, while $(n-m) = \text{const}$ SWNTs form patterns departing from lower intensities up to higher intensities with armchair SWNTs having low intensities and zigzag nanotubes having larger intensities. The (n,m) dependence of the electron-photon matrix elements (see Ref. 46) is weak when compared with the (n,m) dependence of the electron-phonon matrix elements, that dominate the (n,m) dependence for the RRS intensities for the RBM modes.
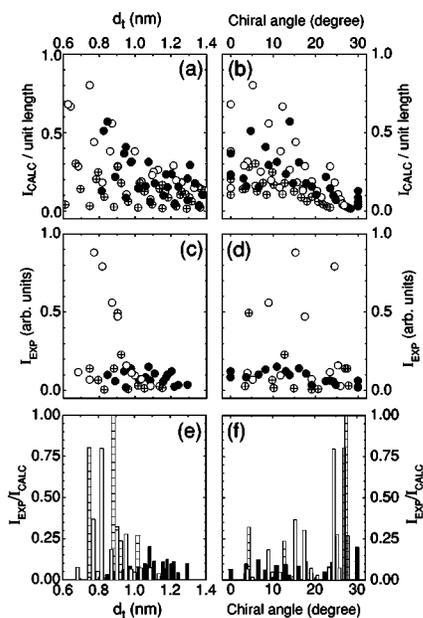
FIG. 8. (a) and (b) show RBM Raman intensity per unit length calculated for each (n,m) SWNT according to Ref. 43, as a function of d_t (a) and θ (b), under the condition of resonance with the incident photon resonance ($E_{\text{laser}}=E_{ii}$). The lifetime is chosen to be $\gamma=60$ meV (Ref. 29). Filled (●), open (○), and crossed circles (⊕), respectively, denote E_{11}^M, E_{22}^S type-I, and E_{22}^S type-II SWNTs. (c) and (d), respectively, show the intensity dependence on d_t and θ, where the RBM peak intensity for each (n,m) SWNT is measured when in resonance with the incident light. (e) and (f), respectively, show the intensity ratio dependence on d_t and θ of the experimentally obtained [I_{EXP}, from (c) and (d)] to the calculated [I_{CALC}, from (a) and (b)] Raman intensities of the radial breathing mode peak for each (n,m) SWNT measured when in resonance with the incident light. Solid, open, and dashed vertical bars stand for metallic, semiconducting type-I and type-II SWNTs, respectively.

In general the calculated intensity is observed to increase with decreasing diameter. The reason for this increase is twofold, (i) the electron-phonon interaction strength for the RBM increases with decreasing diameter, and (ii) there is an increase in the intensity of the DOS singularities with decreasing diameter, since the band curvatures decrease when the vHSs get further from the K point, and the SWNTs get more energy levels per unit energy range for energies where the vHSs are located. This result is consistent with the absence of experimental observation[6] of RBM features for SWNTs with d_t larger than 2 nm.

The electron-phonon matrix elements also depend on chiral angle, and the magnitude of the matrix elements are found to be different for type-I and type-II SWNTs,[44] being generally larger for type-I SWNTs within E_{22}^S. This effect can be understood by mapping E_{ii} in the hexagonal Brillouin zone (BZ). Near the K-M line, $M^{\text{e-ph}}(k)$ decreases with increasing chiral angle, while near the Γ-K line $M^{\text{e-ph}}(k)$ tends to increase with increasing chiral angle. Since E_{22}^S falls on different sides of the BZ with respect to the K point (see Fig. 4) for type-I and type-II semiconducting SWNTs, their intensity behaviors are very different.

In Figs. 8(c) and 8(d) the RRS intensities for the radial breathing mode peaks obtained experimentally for each (n,m) SWNT are plotted as a function of d_t (c) and θ (d). The RBM intensity for each (n,m) SWNT was obtained by fitting the Raman spectra at the respective E_{ii} value, i.e., the intensities plotted in Figs. 8(c) and 8(d) are for resonance with the incident laser light. The intensities for each RBM spectrum are normalized by the Raman intensity of a CCl_4 solution taken with the same E_{laser}, after each RBM measurement. CCl_4 has a band gap larger than 10 eV and can therefore be used for E_{laser}-independent intensity calibration in the visible range. The results shown in Figs. 8(c) and 8(d) can therefore be directly compared with the calculations in Figs. 8(a) and 8(b). It is important to stress that a plot similar to Figs. 8(c) and 8(d) made with the maximum intensity taken at the center of the resonance window (between E_{ii} and $E_{ii}+E_{\text{RBM}}$), rather than at $E_{\text{laser}}=E_{ii}$, gives a similar picture, with only small deviations.

Figure 8(c) shows that the intensities tend to decrease with increasing d_t, and are generally larger for type-I SWNTs in comparison to type-II SWNTs, in agreement with the theoretical predictions shown in Fig. 8(a). For carrying out an analysis of the population of specific (n,m) SWNTs in the sample, the ratio between the experimental and the calculated RBM intensities, as a function of d_t and θ, are shown in Figs. 8(e) and 8(f), respectively. Equal populations for all (n,m) SWNTs in the sample would give a constant ratio for all the tubes, while the real ratio profile should give the (n,m) distribution in the sample.

The first information one gets when comparing Figs. 8(c) and 8(e), or Figs. 8(d) and 8(f), is that the direct comparison of the measured optical intensities does not give the population of specific (n,m) SWNTs in the sample. Figure 8(e) suggests that with the sample preparation process used here, as given by Ref. 16, SWNTs within the diameter range ($0.7<d_t<1.3$ nm) are produced, with a maximum in the diameter distribution occurring at a small d_t value (0.8 nm) rather than exhibiting a symmetric Gaussian distribution, as might be expected from equal *a priori* considerations. From Fig. 8(e) there is an apparent shift of the peak in the SWNT diameter distribution to lower d_t values for semiconducting tubes, and to higher d_t values for metallic tubes. However, this result just reflects the energy range used to measure the data, where larger diameter metallic tubes (E_{11}^M) and smaller diameter semiconducting tubes (E_{22}^S) are selected by the available laser energies. For type-I vs type-II semiconducting SWNTs, 11 tubes of each type have been measured, and in general they exhibit a similar ratio in Figs. 8(e) and 8(f), i.e., type-I and type-II populations are similar at a given d_t.

Finally, Fig. 8(f) shows the chirality dependence of the intensity ratio. Although some chirality dependence can be seen, the effect is not clear due to the mixing of SWNTs with different diameters. Figure 9 shows the chirality dependence of $I_{\text{EXP}}/I_{\text{CALC}}$ for the SWNTs within $0.7<d_t<0.9$ (a) and $0.9<d_t<1.1$ (b). No significant chirality preference for the larger diameter tubes, i.e., SWNTs with d_t above 0.9 nm is observed. However, for the low-diameter tubes (d_t below 0.9 nm), the large chiral angle tubes seem to be preferred. There are three SWNTs in particular that exhibit higher intensities, and these are the (6, 5), (7, 5), and (7, 6) SWNTs, in agreement with results on SWNT samples grown from CoMoCAT[47] or alcohol.[17]
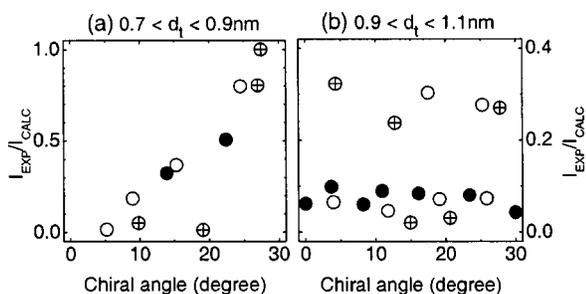
FIG. 9. I_{EXP}/I_{CALC} as a function of chiral angle for SWNTs with $0.7 < d_t < 0.9$ (a) and $0.9 < d_t < 1.1$ (b).

VII. CONCLUSIONS

This paper discusses the electronic transition energies E_{22}^S and E_{11}^M, the ω_{RBM}, and the RBM resonance intensities for SWNTs in the diameter range $0.7 < d_t < 1.3$ nm, based on very accurate RRS experiments on SDS wrapped HiPco SWNTs in an aqueous solution.

(i) For the electronic transitions energies, a theoretical model is applied to fully describe the experimental E_{22}^S and E_{11}^M results within the experimental precision of ± 10 meV. To a first approximation, the extended tight-binding model considering more distant neighbor interactions and nonorthogonality between basis orbitals describes very nicely the general E_{ii} vs (d_t, θ) picture. Many-body effects, i.e., the electron-electron repulsion and the excitonic attraction exhibit a dependence of E_{ii} on both (d_t, θ), i.e., on (n, m). The many-body corrections can, however, be put into a functional form that has a diameter dependence [a logarithmic blueshift of up to 240 meV which goes to zero as $d_t \rightarrow \infty$, Eq. (1)], and a chirality dependence [up to 70 meV, Eqs. (2)–(5)] that takes curvature and trigonal warping effects into account. The chirality effects are extracted in detail from the experimental data for both semiconducting and metallic SWNTs, although rather different chirality-dependent behavior is observed for metallic SWNTs due to the presence of minigap-dependent screening effects that are present in metallic SWNTs and not in semiconducting SWNTs.

The E_{22}^S and E_{11}^M values obtained here are consistent with previously published RRS experimental data on SWNTs. The model is extended to $d_t > 1.2$ nm and $E_{ii} < 1.5$ eV, where there are presently no experimental data available. Experimental results over a wide range of d_t values will be valuable to test the logarithmic correction proposed by KM.[31]

(ii) For the radial breathing mode frequencies, a functional form for $\omega_{RBM}(d_t, \theta)$ was obtained that takes the curvature effect into account explicitly. It is shown that both a $1/d_t^2$ and a chirality dependent term are necessary to reproduce the experimental results within the experimental error. The results nicely reproduce the expectations from theoretical calculations,[27,38] including the chirality dependence and

the differences between metallic and semiconducting SWNTs. The effects of the environment on ω_{RBM} are expected to be on the order of tens of cm^{-1}, and are found to be different for metallic and semiconducting SWNTs. The functional form that is obtained for $\omega_{RBM}(d_t, \theta)$ suggests that the various coefficients in Eq. (6) may be universal except for B, which is the "environmental" term. This interpretation may turn out not to be correct, since the various environments that have been used vary significantly from one another, some environments (e.g., SDS) are elastically soft and others (e.g., a SiO$_2$ substrate) are stiff, some will have extensive charge transfer and others may not. Further theoretical and experimental work is urgently needed for the development of a universal model that accounts for the RBM frequencies of SWNTs in bundles,[9] freely suspended on posts,[48] sitting on a SiO$_2$ substrate,[39] or within the outer wall of a double-wall carbon nanotube,[49,50] etc.

(iii) About the RRS intensity analysis, the development of a reliable method for characterization of the population of (n, m) SWNTs within a sample has been investigated. This work compares the RRS intensities obtained experimentally with calculations based on a tight-binding scheme. The calculated results shed light on a proper interpretation of experimental results, showing that the diameter, chirality and type-I vs type-II semiconducting SWNTs intensity dependencies are not directly related to a real population distribution, but rather to a complicated (n, m) dependence of the various relevant optical processes that must be considered explicitly. Surprisingly, the (6, 5), (7, 5), and (7, 6) SWNTs seem to be more abundant in the HiPco sample used in the present study, suggesting that the enhancement of these specific SWNTs occur not only for CoMoCAT[47] and alcohol[17] samples, but also for HiPco SWNTs. This result can only be obtained after correcting the experimental intensity measurements for each tube with its appropriate RRS cross section. Furthermore, it is seen that while for the very small diameter tubes (d_t below 0.9 nm), the large chiral angle SWNTs seem to be preferred during synthesis, no significant chirality preference is observed for the larger diameter tubes, i.e., SWNTs with d_t above 0.9 nm. This result suggests that when going to very low-diameter tubes, large chiral angle tubes are easier to form, as suggested by Maruyama.[51]

[1] H. Kataura, Y. Kumazawa, Y. Maniwa, I. Umezu, S. Suzuki, Y. Ohtsuka, and Y. Achiba, Synth. Met. **103**, 2555 (1999).

[2] Z. M. Li, Z. K. Tang, H. J. Liu, N. Wang, C. T. Chan, R. Saito, S. Okada, G. D. Li, J. S. Chen, N. Nagasawa, and S. Tsuda, Phys. Rev. Lett. **87**, 127401 (2001).

[3] M. Ichida, S. Mizuno, Y. Saito, H. Kataura, Y. Achiba, and A. Nakamura, Phys. Rev. B **65**, 241407(R) (2002).

[4] A. Hagen, G. Moos, V. Talalaev, and T. Hertel, Appl. Phys. A: Mater. Sci. Process. **78**, 1137 (2004).

[5] M. S. Dresselhaus, G. Dresselhaus, A. Jorio, A. G. Souza Filho, and R. Saito, Carbon **40**, 2043 (2002).

[6] A. Jorio, M. A. Pimenta, A. G. Souza Filho, R. Saito, G. Dresselhaus, and M. S. Dresselhaus, New J. Phys. **5**, 139 (2003).

[7] A. Jorio, R. Saito, M. S. Dresselhaus, and G. Dresselhaus, in *Philosophical Transactions of the Royal Society: Special Issue; Raman Spectroscopy in Carbons: From Nanotubes to Diamond*, edited by Andrea Ferrari and John Robertson (Royal Society, Oxford, UK, 2004), pp. 2311–2336.

[8] L. Alvarez, A. Righi, T. Guillard, S. Rols, E. Anglaret, D. Laplaze, and J.-L. Sauvajol, Chem. Phys. Lett. **316**, 186 (2000).

[9] M. Milnera, J. Kürti, M. Hulman, and H. Kuzmany, Phys. Rev. Lett. **84**, 1324 (2000).

[10] H. Kuzmany, W. Plank, M. Hulman, Ch. Kramberger, A. Grüneis, H. Peterlik, H. Kataura, and Y. Achiba, Eur. Phys. J. B **22**, 307 (2001).

[11] A. Kukovecz, Ch. Kramberger, V. Georgakilas, M. Prato, and H. Kuzmany, Eur. Phys. J. B **28**, 223 (2002).

[12] Ch. Kramberger, R. Pfeiffer, H. Kuzmany, V. Zólyomi, and J. Kürti, Phys. Rev. B **68**, 235404 (2003).

[13] M. S. Strano, S. K. Doorn, E. H. Haroz, C. Kittrell, R. H. Hauge, and R. E. Smalley, Nano Lett. **3**, 1091 (2003).

[14] M. Hulman, R. Pfeiffer, and H. Kuzmany, New J. Phys. **6**, 1 (2004).

[15] M. J. O'Connell, S. Sivaram, and S. K. Doorn, Phys. Rev. B **69**, 235415 (2004).

[16] M. J. O'Connell, S. M. Bachilo, X. B. Huffman, V. C. Moore, M. S. Strano, E. H. Haroz, K. L. Rialon, P. J. Boul, W. H. Noon, C. Kittrell, J. Ma, R. H. Hauge, R. B. Weisman, and R. E. Smalley, Science **297**, 593 (2002).

[17] Y. Miyauchi, S. Chiashi, Y. Murakami, Y. Hayashida, and S. Maruyama, Chem. Phys. Lett. **387**, 198 (2004).

[18] J. Lefebvre, P. Finnie, and Y. Homma, Phys. Rev. B **70**, 045419 (2004).

[19] R. Saito, G. Dresselhaus, and M. S. Dresselhaus, *Physical Properties of Carbon Nanotubes* (Imperial College Press, London, 1998).

[20] S. Reich, C. Thomsen, and J. Maultzsch, *Carbon Nanotubes: Basic Concepts and Physical Properties* (Wiley-VCH, Berlin, 2004).

[21] S. Reich, J. Maultzsch, C. Thomsen, and P. Ordejón, Phys. Rev. B **66**, 035412 (2002).

[22] A. G. Souza Filho, S. G. Chou, Ge. G. Samsonidze, G. Dresselhaus, M. S. Dresselhaus, Lei An, J. Liu, Anna K. Swan, M. S. Ünlü, B. B. Goldberg, A. Jorio, A. Grüneis, and R. Saito, Phys. Rev. B **69**, 115428 (2004).

[23] C. L. Kane and E. J. Mele, Phys. Rev. Lett. **90**, 207401 (2003).

[24] C. D. Spataru, S. Ismail-Beigi, L. X. Benedict, and S. G. Louie, Phys. Rev. Lett. **92**, 077402 (2004).

[25] S. Lebedkin, K. Arnold, F. Hennrich, R. Krupke, B. Renker, and M. M. Kappes, New J. Phys. **5**, 140 (2003).

[26] V. N. Popov, New J. Phys. **6**, 17 (2004).

[27] Ge. G. Samsonidze, R. Saito, N. Kobayashi, A. Grüneis, J. Jiang, A. Jorio, S. G. Chou, G. Dresselhaus, and M. S. Dresselhaus, Appl. Phys. Lett. **85**, 5703 (2004).

[28] D. Porezag, Th. Frauenheim, Th. Köhler, G. Seifert, and R. Kaschner, Phys. Rev. B **51**, 12 947 (1995).

[29] C. Fantini, A. Jorio, M. Souza, M. S. Strano, M. S. Dresselhaus, and M. A. Pimenta, Phys. Rev. Lett. **93**, 147406 (2004).

[30] H. Telg, J. Maultzsch, S. Reich, F. Hennrich, and C. Thomsen, Phys. Rev. Lett. **93**, 177401 (2004).

[31] C. L. Kane and E. J. Mele, Phys. Rev. Lett. **93**, 197402 (2004).

[32] R. Saito, G. Dresselhaus, and M. S. Dresselhaus, Phys. Rev. B **61**, 2981 (2000).

[33] E. Chang, A. Ruini, G. Bussi, and E. Molinari, Phys. Rev. Lett. **92**, 196401 (2004).

[34] V. Perebeinos, J. Tersoff, and Ph. Avouris, Phys. Rev. Lett. **92**, 257402 (2004).

[35] E. V. Condon and G. H. Shortley, *Theory of Atomic Spectra* (Cambridge University Press, Cambridge, England, 1959).

[36] G. D. Mahan, Phys. Rev. B **65**, 235402 (2002).

[37] U. D. Venkateswaran, D. L. Masica, G. U. Sumanasekara, C. A. Furtado, U. J. Kim, and P. C. Eklund, Phys. Rev. B **68**, 241406(R) (2003).

[38] J. Kürti, V. Zólyomi, M. Kertesz, and G. Y. Sun, New J. Phys. **5**, 125 (2003).

[39] A. Jorio, R. Saito, J. H. Hafner, C. M. Lieber, M. Hunter, T. McClure, G. Dresselhaus, and M. S. Dresselhaus, Phys. Rev. Lett. **86**, 1118 (2001).

[40] A. Jorio, A. G. Souza Filho, G. Dresselhaus, M. S. Dresselhaus, A. K. Swan, M. S. Ünlü, B. Goldberg, M. A. Pimenta, J. H. Hafner, C. M. Lieber, and R. Saito, Phys. Rev. B **65**, 155412 (2002).

[41] A. G. Souza Filho, A. Jorio, J. H. Hafner, C. M. Lieber, R. Saito, M. A. Pimenta, G. Dresselhaus, and M. S. Dresselhaus, Phys. Rev. B **63**, 241404(R) (2001).

[42] M. A. Pimenta, A. Marucci, S. Empedocles, M. Bawendi, E. B. Hanlon, A. M. Rao, P. C. Eklund, R. E. Smalley, G. Dresselhaus, and M. S. Dresselhaus, Phys. Rev. B **58**, R16 016 (1998).

[43] R. M. Martin and L. M. Falicov, in *Light Scattering in Solids I*, edited by M. Cardona, Topics in Applied Physics No. 8 (Springer-Verlag, Berlin, 1983), Chap. 3, pp. 79–145.

[44] A. Grüneis, Ph.D. thesis, Tohoku University, Sendai, Japan, 2004.

[45] M. Machón, S. Reich, H. Telg, J. Maultzsch, P. Ordejón, and C. Thomsen, cond-mat/0408436 (unpublished).

[46] A. Grüneis, R. Saito, Ge. G. Samsonidze, T. Kimura, M. A. Pimenta, A. Jorio, A. G. Souza Filho, G. Dresselhaus, and M. S. Dresselhaus, Phys. Rev. B **67**, 165402 (2003).

[47] S. M. Bachilo, L. Balzano, J. E. Herrera, F. Pompeo, D. E. Resasco, and R. B. Weisman, J. Am. Chem. Soc. **125**, 11 186 (2003).

[48] S. B. Cronin, A. K. Swan, M. S. Ünlü, B. B. Goldberg, M. S. Dresselhaus, and M. Tinkham, Phys. Rev. Lett. **93**, 167401 (2004).

[49] R. R. Bacsa, A. Peigney, Ch. Laurent, P. Puech, and W. S. Bacsa, Phys. Rev. B **65**, 161404(R) (2002).

[50] R. Pfeiffer, H. Kuzmany, Ch. Kramberger, Ch. Schaman, T. Pichler, H. Kataura, Y. Achiba, J. Krti, and V. Zlyomi, Phys. Rev. Lett. **90**, 225501 (2003).

[51] S. Maruyama, in International Conference on the Science and Application of Nanotubes, 2004 (unpublished).